Medical Image Analysis 54 (2019) 76–87

Contents lists available at ScienceDirect

Medical Image Analysis

journal homepage: www.elsevier.com/locate/media

Breast MRI and X-ray mammography registration using gradient values

Eloy García[a,*], Yago Diez[b], Oliver Diaz[a], Xavier Lladó[a], Albert Gubern-Mérida[c], Robert Martí[a], Joan Martí[a], Arnau Oliver[a]

[a] Institute of Computer Vision and Robotics, University of Girona, Spain
[b] Department of Mathematical Sciences, Faculty of Science, Yamagata University, Japan
[c] Radboud University Medical Center, Nijmegen 6525GA, The Netherlands

ARTICLE INFO

Article history:
Received 19 November 2017
Revised 21 February 2019
Accepted 22 February 2019
Available online 26 February 2019

Keywords:
Breast cancer
Multimodal registration
X-ray mammography
MRI

ABSTRACT

Breast magnetic resonance imaging (MRI) and X-ray mammography are two image modalities widely used for early detection and diagnosis of breast diseases in women. The combination of these modalities, traditionally done using intensity-based registration algorithms, leads to a more accurate diagnosis and treatment, due to the capability of co-localizing lesions and susceptibles areas between the two image modalities. In this work, we present the first attempt to register breast MRI and X-ray mammographic images using intensity gradients as the similarity measure. Specifically, a patient-specific biomechanical model of the breast, extracted from the MRI image, is used to mimic the mammographic acquisition. The intensity gradients of the glandular tissue are directly projected from the 3D MRI volume to the 2D mammographic space, and two different gradient-based metrics are tested to lead the registration, the normalized cross-correlation of the scalar gradient values and the gradient correlation of the vectoral gradients. We compare these two approaches to an intensity-based algorithm, where the MRI volume is transformed to a synthetic computed tomography (pseudo-CT) image using the partial volume effect obtained by the glandular tissue segmentation performed by means of an Expectation-Maximization algorithm. This allows us to obtain the digitally reconstructed radiographies by a direct intensity projection. The best results are obtained using the scalar gradient approach along with a transversal isotropic material model, obtaining a target registration error (TRE), in millimeters, of 5.65 ± 2.76 for CC- and of 7.83 ± 3.04 for MLO-mammograms, while the TRE is 7.33 ± 3.62 in the 3D MRI. We also evaluate the effect of the glandularity of the breast as well as the landmark position on the TRE, obtaining moderated correlation values (0.65 and 0.77 respectively), concluding that these aspects need to be considered to increase the accuracy in further approaches.

1. Introduction

Breast cancer is the most common cancer in women worldwide. Current statistics have shown that 1 in 8 women will develop invasive breast cancer over the course of her lifetime (BreastCancer.org, 2017). Early detection through imaging increases the likelihood of overcoming the disease, motivating the implementation of screening programs. While X-ray mammography is considered the gold standard image modality for screening and diagnosis of breast diseases, magnetic resonance imaging (MRI) can be used to obtain complementary information, especially for women with an increased risk. For example, MRI can be used to confirm or reject the hypothesis of malignancy of suspicious areas, providing detailed 3D images of the internal tissue of the breast.

This capability of MRI has motivated the investigation of image registration algorithms to correlate information from both image modalities. Traditionally, algorithms based on intensity information have been proposed. A common approach is to extract a biomechanical model of the breast from the MRI volume, to mimic the mammographic acquisition (García et al., 2018a). Ruiter et al. (2006) used the circumference of the mammogram to estimate the shape of the deformed model. Later, Hopp and Ruitter (2012) extended the algorithm, including the rotation of the breast around the anterior-posterior axis. Other methods perform the projection of the internal tissue, including the use of *a posteriori* intensity-based registration approaches such as rigid (Lee et al., 2013), B-spline transformations (Solves-Llorens et al., 2014) or the

* Corresponding author.
E-mail address: eloy.garcia@eia.udg.edu (E. García).

https://doi.org/10.1016/j.media.2019.02.013

Demons algorithm (García et al., 2015). Hopp et al. (2013) introduced a 3D-2D intensity-based registration approach that consists of optimizing a number of parameters such as position and orientation of the model, to adapt the registration process to the patient-specific conditions. Similarly, Mertzanidou et al. (2014) included the elastic parameters as well as the amount of compression in the optimization and allowed the breast model to rotate in the anterior-posterior and superior-inferior axis.

These approaches perform the projection of the internal tissue of the breast from the 3D MRI -i.e. compressed model- to the 2D-mammographic space. However, due to the physics underlying each modality, there is no correlation between the voxel intensities in X-ray and MRI images for each tissue. Therefore, intensity-based registration algorithms require an additional step, which is the segmentation of the internal tissue of the breast in the MRI volume. The accuracy of the registration may be subjected to the suitability of the segmentation algorithm. Conversely, the voxel intensities in computed tomography (CT) data are related to the X-ray linear attenuation coefficient by means of the Hounsfield units and, consequently, several registration algorithms have proposed generating pseudo-CT data from the MRI volumes (Van der Bom et al., 2011). Nevertheless, the voxel intensity transformation also depends on establishing a suitable correspondence between the MRI and CT voxel intensities.

Furthermore, to overcome these issues, feature- and gradient-based methods have been proposed to perform the multimodal image registration (Gan et al., 2008) or to combine these properties with intensity-based approaches (Pluim et al., 2000). Specifically, 3D-2D gradient-based registration approaches have been proposed for image-guided interventions. Tomaževič et al. (2003) introduced a gradient-based algorithm to register CT and MRI to X-ray images. The registration looks for the rigid transformation of the body part, in this case the lumbar spine, which provides the best match between surface normals and backprojected gradients, considering their amplitudes and orientations. Similarly, Livyatan et al. (2003) proposed a gradient-based method in which only the edges of the 2D images were used to compute the transformation of the gradient field extracted from the 3D images. Finally, Markelj et al. (2008) combined a gradient- and reconstruction-based approach to obtain a 2D-3D registration method for CT and MRI images.

These approaches are based on back-projecting the ray from the 2D image and evaluating the intersection of the ray with respect to the 3D body surface. However, the gradient information can also be projected from the 3D volume to the 2D image. Mertzanidou et al. (2010) used an affine transformation to generate synthetic mammograms. Gradient values of the synthetic mammograms are extracted a posteriori and used to lead the registration. Furthermore, Hopp et al. (2012) performed the fusion of information between ultrasound computed tomography (3D) and X-ray mammography using a patient-specific FEM biomechanical model and gradient-based metrics. The 3D image was modified by means of a deformation field extracted from the FE analysis and the internal tissues were projected in order to obtain a synthetic image. Similar to the previous case, gradient values were extracted a posteriori and used to lead the registration. On the other hand, Wein et al. (2005) proposed a 3D-2D algorithm in which the gradients of the 3D image are directly projected and compared to the information belonging to the 2D image. Furthermore, Wein et al. also defined a gradient ray-casting and gradient correlation metric to perform the registration.

In this paper, we introduce two gradient-based registration approaches with the aim of correlating the information contained in the breast MRI and the X-ray mammogram. To our knowledge, this is the first attempt to introduce a gradient-based approach performing the gradient projection directly from the MRI without modifying the initial volume. These methods do not require the segmentation of the internal tissues of the breast. During the registration between MRI and mammography, a finite element (FE) biomechanical model, extracted from the MRI volume, is highly compressed, mimicking the mammographic acquisition. Therefore, conversely to previous 3D-2D gradient-based algorithms, the registration cannot be considered as a rigid transformation of the 3D volume. Furthermore, while the FE model is compressed, the MRI volume is not deformed to avoid the loss of information. Tissue gradients from the MRI volume are directly projected into the 2D mammographic space using a uniform grid to speed up the ray-casting and directly obtaining the gradient values from the uncompressed 3D image volume. The projected gradients and those obtained in the mammograms are compared in two different ways. On the one hand, only the scalar gradient values are compared using normalized cross-correlation (NCC), while on the other hand, each direction is independently considered, obtaining a gradient vector that is compared to the directional derivative of the mammogram using a gradient correlation (GC) metric. Finally, the results of these registration algorithms are compared to an intensity-based approach where the MRI is transformed to a pseudo-CT image, using a polyenergetic spectrum simulated by means of considering the corresponding end-point energy spectrum (KVP) recorded in the DICOM header of the mammogram to obtain a case-specific simulation. Glandular and adipose tissue are segmented using an Expectation-Maximization (EM) algorithm, and NCC is used to guide the registration.

In addition, the performance of isotropic and anisotropic material models is evaluated, considering several factors of interest such as the breast glandularity and the internal landmark position. To provide a fair comparison, we propose a semiautomatic approach to isolate the landmarks in both, MRI and mammography, to reduce the intra- and inter-observer variability that can be introduced using a manual segmentation. Furthermore, we propose an internal system of reference within the mammograms to localize the lesions.

2. Methodology

Based on our previous work (García et al., 2018b), we have developed a fully automatic 3D-2D gradient-based framework to register MRI to X-ray mammograms. In contrast to that work, in this paper we directly use for presentation FFDM to lead the registration process. The biomechanical model extraction as well the optimization step are similar in the two works. However, in this case, three similarity metrics -an intensity-based approach versus two gradient-based approaches- are tested. The intensity-based approach provides us a baseline result to evaluate the behavior of the gradient-based algorithms. Fig. 1 summarizes the registration approaches, and the following sections provide a detailed description of the process.

2.1. Mechanical modeling

Patient-specific biomechanical models require an accurate geometrical description of the breast. The biomechanical model extraction presented is similar to that introduced in our previous work (García et al., 2018b). The models are built from pre-contrast T1-weighted MR images. The approach proposed by Gubern-Mérida et al. (2012) is used to separate each breast. A probabilistic atlas approach, which contains spatial information of pectoral muscle, lungs, heart, thorax and breast tissue, is used in the MRI volumes to exclude the body from the breast. Then, the breast mask is resampled to isotropic voxels of 5.0 mm length and the surface mesh is extracted using the marching cubes algorithm

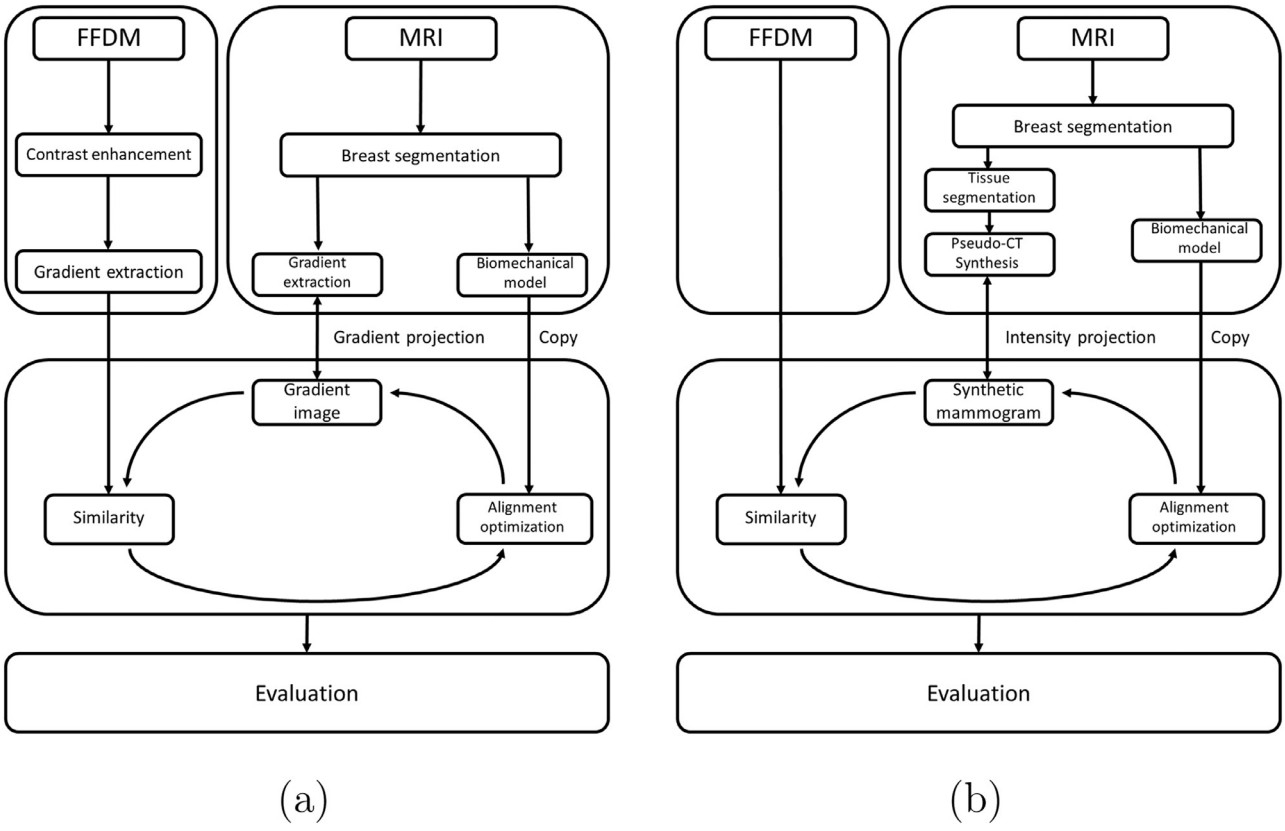

Fig. 1. Scheme of the gradient- (a) and intensity-based (b) registration processes. The breast model is built from the MRI, and compressed mimicking the mammographic acquisition. Depending on the approach, gradient or intensity values are projected from the MRI to the mammogram and used in the similarity measure to perform the alignment optimization of the model.

(Lorensen and Cline, 1987). Nodes belonging to the breast-body interface are automatically selected, using morphological filters and logical operations, and are fitted to a linear surface (García et al., 2018b). The surface mesh is smoothed using a Lagrangian smoothing process (Herrmann, 1976), and the volume mesh is extracted by means of the open-source package TetGen[1] (Si, 2015), using a maximum volume criterion to generate the tetrahedral elements. The number of elements composing the biomechanical model is between 50k and 200k elements (105, 288 ± 45, 952 on average), depending on the breast volume.

Usually, living tissues are described assuming a non-linear behavior (Fung, 1993). In this work, both isotropic and anisotropic -i.e. transversal isotropic- hyperelastic Neo-Hookean material models (Han et al., 2012) were tested. The anisotropic behavior was considered to simulate the presence of Cooper's ligaments and connective tissue in the breast. Cooperâ;;s ligaments maintain the structural integrity of the breast establishing a restriction of the movement. This binding condition is simulated, in our case, using the transversal isotropic material. The behavior of hyperelastic materials is described by means of a scalar potential, ψ. Formally, the stress–strain potential of an anisotropic -i.e. transversal isotropic- material is expressed as follows:

$$\psi = \psi_{iso} + \psi_{transv} \tag{1}$$

where, ψ_{iso} represents the isotropic Neo-Hookean material model and ψ_{transv} is the anisotropic term. These terms are defined as follows:

$$\psi_{iso} = \frac{1}{2}\mu(I_1 - 3) + \frac{1}{2}\kappa(J-1)^2 \tag{2a}$$

$$\psi_{transv} = \frac{\eta}{2}(I_4 - 1)^2 \tag{2b}$$

where μ and κ are the shear and bulk moduli and η is an additional material parameter that controls stiffness in a preferred direction. The parameter η is related to the Young's modulus, E, by means of the stiffness anisotropy ratio, $\rho = \frac{\eta}{E}$. When $\rho > 0$, the material is stiffer in one specified direction $\bar{a} = [a_x, a_y, a_z]$. Furthermore, the material description is related to the principal invariants. I_1 represents the first invariant of the right Cauchy-Green tensor C ($C = F'F$ where F is the deformation gradient tensor) and is defined as the trace of C. Furthermore, I_4 is the pseudo invariant of the modified right Cauchy-Green deformation tensor and J represents the ratio between the volume before and after the transformation (Bonet and Wood, 1997).

The constitutive elastic values, Young's modulus and Poisson's ratio, as well as the anisotropic ratio values, are exposed in Section 2.2. In the case of using the transversal isotropic material description, the stiffest direction is defined in the direction perpendicular to the pectoral muscle. The pectoral muscle in the mammograms is excluded using the algorithm proposed by Kwok et al. (2004).

Regarding the boundary conditions of the biomechanical model, from an anatomical point of view, the breast is not rigidly fixed to the body. They are joined by means of connective tissue, allowing the breast to slightly slide along the thorax. Therefore, nodes belonging to the breast-body interface may slide in the direction parallel to the displacement of the paddles (Mertzanidou et al., 2014; Chung, 2008). The contact between the biomechanical breast model and paddles is defined using a frictionless contact model. Skin and gravity are not considered due to the small effect that

[1] http://wias-berlin.de/software/tetgen/.

they have in the simulation (Azar et al., 2001; Ruiter et al., 2006). The open-source package NiftySim™ (Johnsen et al., 2014) (University College London[2]) was used to perform the FE analysis.

2.2. Optimization

The elastic parameters, as well as the position and orientation of the breast model, are optimized using the simulated annealing algorithm (Kirkpatrick and Vecchi, 1983). The optimization consists of finding the maximum value of the corresponding metric. The parameters defined to optimize the alignment are as follows:

- Position: translation of the model along a plane parallel to the mammogram.
- Orientation: the model is allowed to rotate around its principal axes, describing this movement by means of Euler angles, using the notation Roll-Pitch-Yaw (RPY).
- Elastic parameters: Young's modulus, E, and the anisotropy ratio, ρ (when the transversal isotropic material model is considered).
- Amount of compression: the breast thickness.

Eventually, uncompressed and compressed models of the breast are available. The former relates the physical space of the MRI, while the compressed model is localized above the space defined by the mammogram.

Regarding the material description, the elastic parameters measured by Wellman (1999) are taken as a reference to define the mechanical behavior. The search space of the Young's modulus is defined between $E = 4.46$ kPa (the breast is composed of adipose tissue) and $E = 15.1$ kPa (the breast is defined as fully composed of glandular tissue) at Strain= 0.0 % (Tanner et al., 2001). The starting Young's modulus value is defined in the center of the interval, $E = 9.75$ kPa. Furthermore, the Poisson's ratio is considered constant, with value $\nu = 0.495$. Previous experiments show that the best performance is obtained using small anisotropy ratio values. Therefore, we defined the search space of ρ in the interval [0,20], initialized as $\rho = 10$, when the anisotropic term is needed.

The initial position of the biomechanical model is determined by situating its center of mass on the centroid of the breast in the mammogram. The importance of the manual interaction of the radiographer, to situate the breast on the support, has not been evaluated. To reduce the computational cost during the registration, we assume that the breast is well situated to perform the compression by effect of the MRI acquisition, avoiding the computation of the unloaded reference state (García et al., 2018b). Notice that this is an idealized assumption and the computation of the unloaded state is well established in other works (Eiben et al., 2014). Furthermore, when MLO projections are simulated, the pectoral muscle is also used as a reference to situate the model. The search space of the position is determined by the bounding box of the breast in the mammogram. The orientation of the model is initialized using the appropriate DICOM tags header. For the left (right) breast, the model is rotated counter-clockwise (clockwise) to the positioner primary angle recorded, allowing the use of the axis-oriented bounding box of the model to situate the compression plates. During the optimization, Euler angles are limited to small variations ($[-15, 15]$ degrees) with respect to the reference state. The search space of the breast thickness is delimited to variations with respect to the recorded value in the mammogram header (between 0.75 and 1.25 times this value), which is defined as the initial value during the optimization. The simulated annealing algorithm stops after 50 simulations without improvement from the last maximum value of the corresponding metric.

[2] https://sourceforge.net/projects/niftysim/.

2.3. Ray tracing and projection

While the transformation of the biomechanical model is the same in all the cases, we use three different similarity metrics. The first metric corresponds to the traditional intensity-based approach, where the MRI volume is transformed to a pseudo-CT image by means of the tissue segmentation, and NCC is used to lead the registration (Mertzanidou et al., 2012). The other two methods correspond to gradient-based approaches (Wein et al., 2005). First, the directional derivative -i.e. intensity gradients- of both the MRI volume and the corresponding mammogram are computed. The MRI gradients are projected and compared to those obtained in the mammogram. On one hand, the gradient modulus is accumulated along each ray, during the ray-casting and compared to the norm of the intensity gradients belonging to the corresponding mammogram using NCC. On the other hand, the gradients are accumulated along each ray, considering each direction x, y and z independently and the resulting vector, and the intensity gradients obtained from the mammogram are compared using a GC metric.

Thus, to preserve the information contained in the image, the MRI volume is not modified. First, an uniform grid (Lagae and Dutré, 2008) is used to store the information, indexing the elements of the biomechanical model. Hence, the position of the sampled points along the ray can be localized simultaneously in the compressed model and the 3D volume, computing the barycentric coordinates within the elements traversed by the ray. The process performed to localize a given path between both the compressed and the uncompressed model is described in our previous work (García et al., 2018b). All points belonging to one ray in the compressed breast model corresponds to the uncompressed model, obtaining the curve $\gamma(t)$ in the initial volume. This curve is used to integrate the information (voxel intensities or gradients, depending on the algorithm). In the following sections, we describe the 3D-2D projection.

2.3.1. Intensity values projection

To avoid complex synthesis approaches of the mammographic images, the MRI volume is transformed to a pseudo-CT volume (Mertzanidou et al., 2012). First, the internal tissues of the breast (adipose and glandular) are segmented using an Expectation-Maximization (EM) algorithm. Notice that the information -i.e. the amount of glandular tissue- extracted from the MRI is similar to the information contained in the mammograms (García et al., 2017). Instead of just using the effective attenuation coefficient for both glandular and adipose tissue, we propose simulating the X-ray spectrum, using the information contained in the mammographic DICOM header tags, obtaining a case-specific pseudo-CT image for each mammogram. Thus, the images are transformed using the weighted average of the Hounsfield scale (HU), considering the partial voxel effect of the segmentation. Weights are computed by means of the energy spectrum of the corresponding anode material between 0 keV and the end-point energy (kVp) recorded in the mammogram DICOM header. Formally, the synthesis of the pseudo-CT images is expressed as follows:

$$HU = 1000 \cdot \sum_{E=0}^{E=kVp} \omega(E) \frac{\mu_{eff}(E) - \mu_{H_2O}(E)}{\mu_{H_2O}(E) - \mu_{Air}(E)} \tag{3}$$

where $\omega(E)$ represents the normalized weight of the polyenergetic spectrum, and $\mu_{H_2O}(E)$ and $\mu_{Air}(E)$ are the water and air attenuation coefficients at a given energy, E. Moreover, $\mu_{eff}(E)$ represents the "effective" attenuation coefficient, considering the previous segmentation:

$$\mu_{eff}(E) = \mu_{fat}(E) \cdot L_{fat} + \mu_{gland}(E) \cdot L_{gland} \tag{4}$$

where μ_{fat} and μ_{gland} are the adipose and glandular tissue attenuation coefficients, while L_{fat} and L_{gland} are the likelihood of the

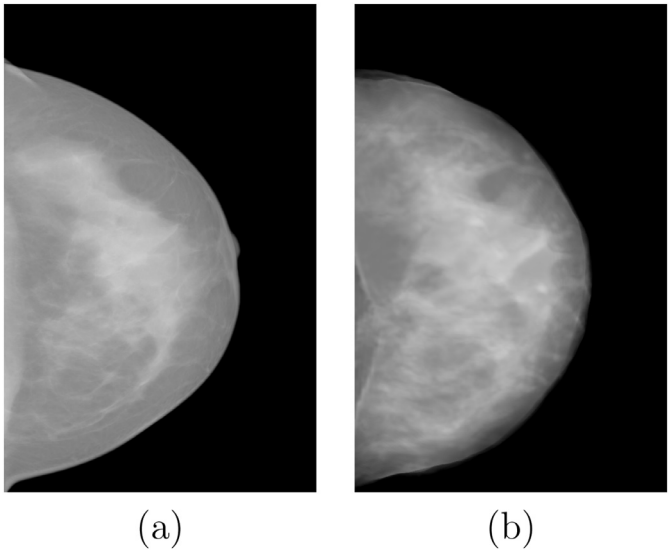

Fig. 2. (a) Real and (b) synthetic mammogram obtained using the intensity-based registration algorithm by means of converting the MRI volume to a pseudo-CT image. In this case, the anode is composed of rhodium and the end-point energy $kVp = 31$ keV.

voxel to belong to the adipose and glandular tissue class, respectively, obtained using the EM algorithm.

The attenuation coefficients, belonging to each tissue and material, are obtained from the NIST (National Institute of Standards and Technology, U.S.) database,[3] while the energy spectra are simulated using the RASMIP (Rhodium Anode Spectral Model-) and MASMIP (Molybdenum Anode Spectral Model using Interpolating Polynomials)[4] models proposed by Boone et al. (1997). Notice that using this approach, signal degradation effects such as photon scattering are not considered. Fig. 2 shows an example of the real and synthetic mammograms obtained by means of transforming the MRI volume to the pseudo-CT image. Using this transformation, the synthesis of a simulated mammogram is performed using a simple digital reconstructed radiograph (DRR) algorithm, avoiding more complex simulations. The intensity values are accumulated along the curve $\gamma(t)$ in the uncompressed model and directly from the pseudo-CT image. Eventually, pixel intensities in the synthetic mammogram are rescaled to the same interval of the original mammogram, and NCC is used to guide the registration.

2.3.2. Absolute gradient projection

To evaluate the gradient similarity, first, the directional derivative is computed in the MRI and the mammogram using the gradient operator:

$$\nabla I = (\partial_x I,\ \partial_y I,\ \partial_z I) \tag{5}$$

where $\partial_x I$, $\partial_y I$ and $\partial_z I$ represent the partial derivative of the image I for the corresponding Cartesian direction. Notice that in the MRI volume, the 3D gradient image is computed, while in the mammogram only $x-$ and $y-$ directions are necessary, with z as the main direction of the projection during the ray casting. In the MRI, the glandular tissue gradients are isolated using the whole breast segmentation exposed in Section 2.1. Similarly, in the mammograms, the breast area is isolated using a threshold approach (Otsu, 1975). After extracting these masks, the background is dilated by a spherical (disk) kernel in 3D (2D) with radius $R = 2.5$ mm. Thus, the breast-body and breast-air gradient interfaces are removed.

The 3D gradients can be projected into the 2D space, integrating the directional derivative along a ray. This line integral is formally expressed as follows:

$$I_G = \int_\gamma V(\vec{\mathbf{r}}) \cdot \mathrm{d}\boldsymbol{l} = \int_a^b V(\gamma(t)) \cdot \dot{\gamma}(t)\ \mathrm{d}t. \tag{6}$$

where $V = \nabla I$ represents the vector field (i.e. 3D gradient image), $\gamma(t)$ is the parametric curve between the points a and b, and $\dot{\gamma}(t)$ represents the derivative of the curve with respect to the parametric term, t. Using the line integral exposed in the Eq. (6), which is widely used in physics to integrate vector fields along a path, the resulting gradient is represented by a scalar value. Therefore, the projected image represents the accumulated gradients of the projection. NCC is used to compute the similarity between this image and the norm of the directional derivative belonging to the corresponding mammogram.

2.3.3. Vectorial gradient projection

The directional derivatives can be considered independently for each direction, as it is exposed by Wein et al. (2005). Thus, the accumulated gradient is formally expressed as follows:

$$\vec{G} = \left(\sum_x |\ I_G\ |\ \vec{u_x}, \sum_y |\ I_G\ |\ \vec{u_y}, \sum_z |\ I_G\ |\ \vec{u_z} \right) \tag{7}$$

where I_G is the line integral of the directional derivative of the MRI volume, using Eq. (6), and $\vec{u_x}$, $\vec{u_y}$ and $\vec{u_z}$ represent the normal vector for the directional derivative at each point, i, in the $x-$, $y-$ and $z-$ directions, respectively. NCC can be computed using the accumulated gradients for the direction x and y and compared using a gradient correlation metric, which is defined as follows:

$$GC = \frac{1}{2}(NCC(\nabla_x(I_1), \nabla_x(I_2)) + \frac{1}{2}(NCC(\nabla_y(I_1), \nabla_y(I_2)) \tag{8}$$

where $NCC(\nabla_x(I_1), \nabla_x(I_2))$ and $NCC(\nabla_y(I_1), \nabla_y(I_2))$ represent the cross-correlation between the gradient images in the x and y direction, respectively.

2.4. Implementation details

Our registration framework was developed in C++, using the Insight Toolkit (ITK v.4.8.0) and the Visualization Toolkit (VTK v.6.1.0) Libraries. The FE simulation as well as the ray casting algorithm were accelerated in GPU using a CUDA implementation. One single compression spends between 10 s and one minute, using 128 threads (default value for NiftySim™). The total time observed for the registration process ranged between 30 min and 3 h (mean: 60.89 ± 39.51 min) on a workstation Intel Core i7-3770 3.40 GHz, RAM 32 Gb, 64 bits equipped with a GPU NVIDIA GeForce GTX 770 (2 Gb).

3. Experimental results

The dataset was composed of 10 clinical cases from 10 different patients. This value is in range with previous works in MRI-mammography registration (Ruiter et al., 2003; Lee et al., 2013; Solves-Llorens et al., 2014; Mertzanidou et al., 2014). Each case contains 1 MRI volume and 1 mammographic study, composed of both CC and MLO projections of the corresponding breast. Notice that only one breast per patient is analyzed. Patients aged between 37 and 63 years (49.2 ± 9.52 years old, in average). Images were acquired at the Radboud University Medical Center (Nijmegen, The Netherlands) between July, 2008, and May, 2011. Both MRI and mammographic studies were acquired in the same day.

[3] https://www.nist.gov.

[4] The anode material in the GE Senographe mammographic device is composed of Rhodium or Molybdenum. Notice that a mammographic device developed by other companies may use different materials, such as Tungsten.

Table 1
Target registration error, in millimeters, for the 10 CC-mammograms, using an isotropic material model.

	c1	c2	c3	c4	c5	c6	c7	c8	c9	c10	mean	std
Intensity	12.73	13.22	7.08	13.28	14.39	2.12	6.45	6.17	10.16	4.64	9.02	4.28
scalar Grad.	12.92	2.23	3.62	3.37	18.53	5.53	4.59	5.13	4.09	10.26	7.03	5.23
vect. Grad.	10.35	6.04	17.31	7.39	11.48	15.27	14.77	11.01	5.02	4.18	10.28	4.57

The MRI scanner used was a 1.5 Tesla Siemens scanner (Magnetom Vision, Magnetom Avanto and Magnetom Trio) with dedicated breast coil (CP Breast Array, Siemens, Erlangen). MRI volumes had a size of $[512 \times 256 \times 120]$ voxels and $[0.664 \times 0.664 \times 1.300]$ mm^3 per voxel. Regarding the mammographic device, the images were acquired by either a GE Senographe 2000D or GE Senographe DS, according to the standard clinical settings. Mammograms were composed of $[2294 \times 1914]$ pixels, with $[0.094 \times 0.094]$ mm^2 per pixel. However, they were resampled to isotropic pixels with 0.3 mm length to increase the similarity to the MRI voxel size. Furthermore, a histogram equalization was applied to them to increase the contrast of the glandular tissue with respect to the adipose tissue.

3.1. Evaluation

The target registration error (TRE) metric is used to evaluate the accuracy of the proposed methods. Each patient contains one single landmark within the breast. Specifically, 8 cases contained biopsy markers -i.e. small metal clips- while 2 cases (corresponding to c2 and c3 in the following sections) contained a clearly visible lesion in the breast. However, the histological results are unknown. Notice that the elastic properties are different for healthy and unhealthy tissues (Wellman, 1999), and they should be balanced.

These landmarks were isolated using a semi-automatic approach to avoid subjective labels and, thus, the intra- and inter-observer variability. In the mammogram, the marker clips are clearly visible as small bright spots, while the MRI yields magnetic susceptibility artifacts that are visually seen as a small black bubble (Fiaschetti et al., 2013). Fig. 3 shows an example of the visualization of these markers in both MRI and mammography. Regarding the breast lesions, they are brighter and clearly visible in the mammograms, while the lesion position in the MRI was localized in the difference image between two time points of the Dynamic Contrast Enhancement (DCE) MRI. Fig. 4 shows an example of the lesion as well as the maximum intensity projection (MIP) of the difference image. The landmarks are localized using red arrows in all the figures.

Isolating the landmarks presented in the "for presentation" mammograms is performed using a threshold approach, 0.85 times the maximum intensity value, based on previous experiments. In the MRI, the magnetic field distortion (i.e. black bubble) and the lesion are located by an expert researcher and marked manually. This point is used as the seed of a region growing algorithm to segment the volume of these landmarks. The TRE is computed as the Euclidean distance between the centroid of the 2D landmark in the mammogram and the projected centroid of the 3D landmark. The centroid of the 3D landmark is moved from the uncompressed to the compressed model using the barycentric coordinates of the corresponding tetrahedral element in the biomechanical model. Then, this point is projected using perspective ray-tracing.

3.2. Results

First, we evaluate the behavior of the isotropic material model. Tables 1 and 2 summarize the TRE results for CC- and MLO-projections, respectively, using the three registration approaches. The intensity-based 3D-2D algorithm provides a baseline result to evaluate the behavior of the proposed gradient-based registration algorithms. Notice that there is not a standard database and one should be cautious comparing the results provided by previous work. However, in this case, we use a set of images and a semi-automatic lesion segmentation to perform a fair comparison among the traditional and the proposed methodology. In the CC cases, the intensity-based approach obtains a mean TRE equal to 9.02 ± 4.28 mm. The higher TRE value corresponds to the value obtained using the vectorial gradient values (10.28 ± 4.57) while, using scalar gradient values the result is 7.03 ± 5.23 mm, on average. In the MLO cases, the two gradient-based methods obtain better results than the intensity-based method (12.96 ± 3.78 mm). The best result is obtained using scalar gradient values (9.67 ± 5.80 mm).

Considering each case independently, most of the TREs are lower than 15 mm. In several cases, such as *c*3, *c*5 and *c*6, the TRE depends on the algorithm. For instance, the patient *c*6 ob-

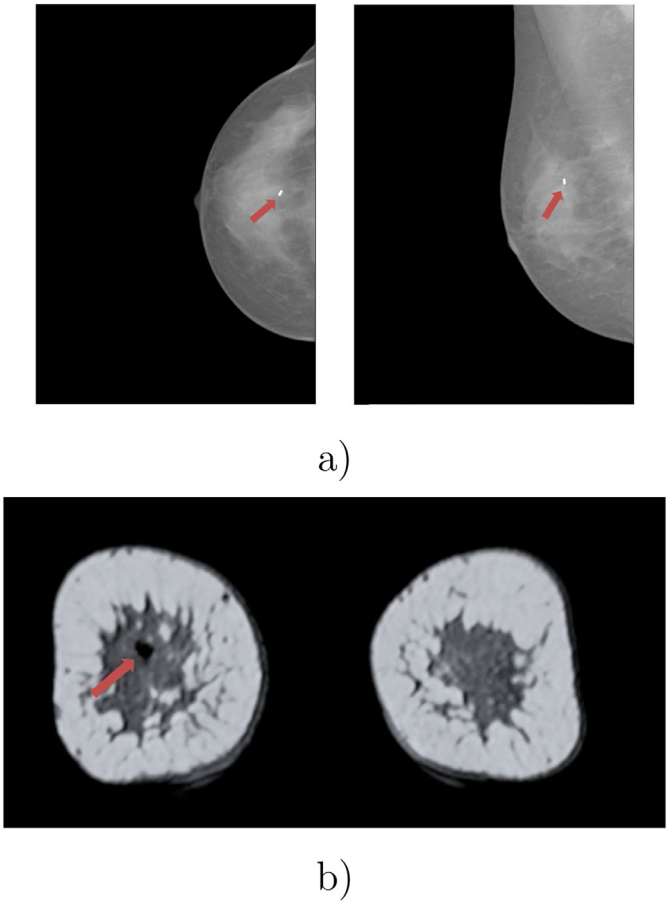

Fig. 3. Metallic clip for image-guided biopsy. The clip is visible in (a) CC and MLO mammograms as a bright spot, while in (b) MRI it yields a magnetic susceptibility artifact, which is visually seen as a small black bubble. The landmark position is shown using a red arrow in the images. (For interpretation of the references to colour in this figure legend, the reader is referred to the web version of this article.)

Table 2
Target registration error, in millimeters, for the 10 MLO-mammograms, using an isotropic material model.

	c1	c2	c3	c4	c5	c6	c7	c8	c9	c10	mean	std
Intensity	13.97	10.30	9.14	8.45	19.79	17.12	13.27	16.08	9.76	11.67	12.96	3.78
scalar Grad.	12.03	16.22	19.65	3.28	15.12	8.00	8.40	3.49	4.08	6.44	9.67	5.80
vect. Grad.	7.61	12.08	16.02	13.51	9.36	16.33	21.18	13.10	3.41	12.04	12.46	4.95

Table 3
Target registration error, in millimeters, for the 10 CC-mammograms, using a transversal isotropic material model.

	c1	c2	c3	c4	c5	c6	c7	c8	c9	c10	mean	std
Intensity	13.10	9.44	2.32	15.10	4.13	6.65	4.79	4.17	4.86	14.50	7.90	4.76
scalar Grad.	9.38	2.37	6.46	3.74	2.56	9.39	8.73	4.54	3.34	5.95	5.65	2.76
vect. Grad	9.81	4.56	11.36	9.85	13.45	8.25	14.84	12.37	7.47	3.60	9.56	3.67

Table 4
Target registration error, in millimeters, for the 10 MLO-mammograms, using a transversal isotropic material model.

	c1	c2	c3	c4	c5	c6	c7	c8	c9	c10	mean	std
Intensity	13.00	8.62	6.52	7.86	5.56	17.60	15.50	5.38	7.11	12.50	9.96	4.35
scalar Grad.	10.53	9.88	11.37	8.68	10.41	5.37	9.16	6.36	3.22	3.31	7.83	3.04
vect. Grad.	6.54	10.39	15.10	8.02	11.57	25.44	16.33	13.53	4.56	11.51	12.3	5.91

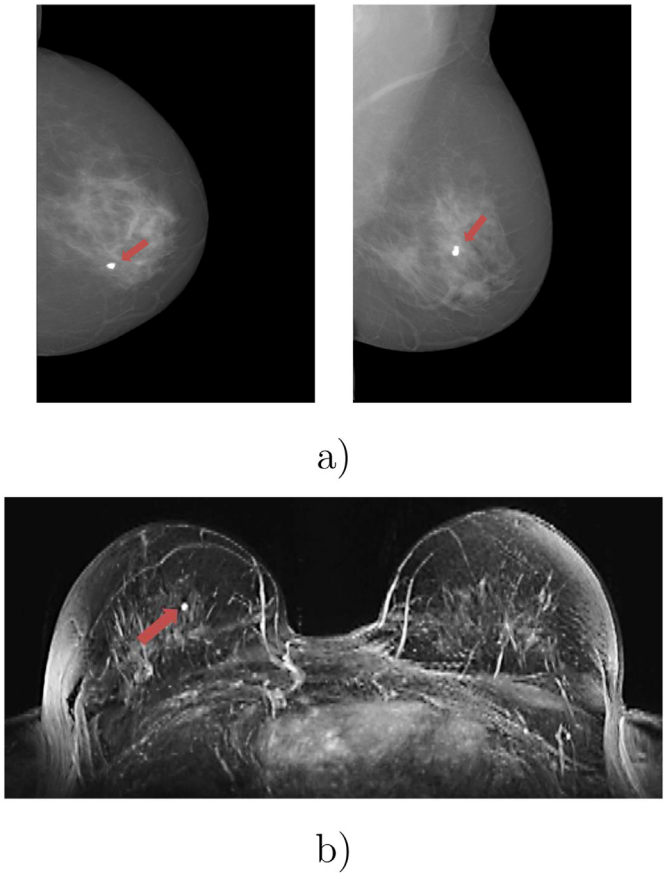

Fig. 4. Lesion in (a) CC and MLO mammograms and (b) the maximum intensity projection of the lesion in the DCE-MRI. The lesion position is localized using a red arrow in the images. (For interpretation of the references to colour in this figure legend, the reader is referred to the web version of this article.)

tains a good performance using scalar gradient values for both CC- and MLO-projections. However, the intensity-based algorithm obtains a good result for CC- but not for MLO-projections. Finally, the method using vectorial gradient values obtains a poor performance in the two cases, with TRE larger than 15 mm.

Furthermore, we test the behavior of the transversal isotropic material model applied to the registration. Tables 3 and 4 collect the TRE results using an anisotropic mechanical model. Like the isotropic model, the best result is obtained using the scalar gradient values for both CC- (5.65 ± 2.76 mm) and MLO- (7.83 ± 3.04 mm) projections, while the worst performance is obtained using vectorial gradient values (9.56 ± 3.67 mm for CC- and 12.30 ± 5.91 mm for MLO-projections).

Comparing the results of both isotropic and anisotropic material models, the TRE obtained using the transversal isotropic material model is lower than the TRE obtained using just the isotropic model. The TRE for the intensity-based method is reduced from 9.02 to 7.90 mm for CC- and from 12.96 mm to 9.96 mm for MLO-mammograms. A similar result is obtained using scalar gradient values. For the CC images, the TRE is reduced from 7.03 to 5.65 mm, while for MLO images, the TRE is reduced from 9.67 to 7.83 mm. Nevertheless, the method that uses vectorial gradient values does not obtain such an improvement. For the CC-case, the vectoral gradients method obtains a better performance using the anisotropic material model, 9.56 mm with respect to 10.28 mm using the isotropic material model, while for MLO images, the TRE barely varies the value (from 12.46 to 12.30 mm).

3.3. Breast contour comparison

In most of the previous works, one single landmark was used to evaluate the accuracy of the registration algorithms. This evaluation may seem rather simplistic, however extracting and matching internal landmarks of the breast is a challenging task due to the difference between the image modalities and the dimension (3D and 2D) of the corresponding images. Nevertheless, to provide a more complete evaluation, we compute the similarities between both the projected and the real breast contours while considering the two material models. Fig. 5 shows the breast mask, obtained from the mammograms, and the contour for both the isotropic (in blue) and the anisotropic (in red) material model.

To quantitatively evaluate the similarity, we use the Hausdorff distance between the two curves. The Hausdorff distance is the largest of all the distances from a point in one set to the closest point in the other set. Mathematically, the Hausdorff distance is defined as follows:

$$H(C_1, C_2) = \max \left\{ \sup_{x \in C_1} \inf_{y \in C_2} \mathrm{d}(x, y), \sup_{y \in C_2} \inf_{x \in C_1} \mathrm{d}(x, y) \right\} \quad (9)$$

Table 5
3D Target registration error, in millimeters, within the MRI, using an isotropic material model.

	c1	c2	c3	c4	c5	c6	c7	c8	c9	c10	mean	std
Intensity	9.67	11.39	8.22	13.37	14.72	12.97	13.63	12.18	6.57	8.16	11.09	2.77
scalar Grad.	15.95	17.45	21.25	1.66	16.25	5.95	5.89	4.64	1.99	10.24	10.13	7.09
vect. Grad.	7.59	10.41	11.65	10.13	7.94	19.21	23.64	7.60	3.36	4.74	10.63	6.30

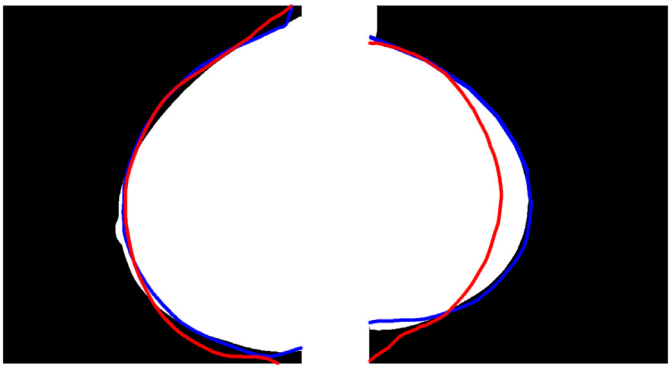

(a) (b)

Fig. 5. Projected breast contours obtained using an isotropic (blue) and anisotropic (red) breast model. Note that in (a) the anisotropic term is close to zero, obtaining a contour similar to that obtained using an isotropic breast model, while in (b) the breast shape obtained using a transversal isotropic material model is different from the breast shape obtained using the isotropic model. (For interpretation of the references to colour in this figure legend, the reader is referred to the web version of this article.)

where x and y represent the points corresponding to the real and projected contours, C_1 and C_2 respectively, and *sup* represents the supremum and *inf* the infimum of the distance $d(x, y)$, in this case, the Euclidean distance.

Fig. 6 shows the results obtained for all the registration algorithms, considering the CC- and MLO-projections independently. Similar to the previous section, the distance between the two curves is smaller (on average) for the algorithm using the absolute gradient values. However, the biomechanical model behavior differs with respect to the material model. In most of the cases, the average of the distribution is smaller for isotropic material models than for the anisotropic models.

3.4. 3D Evaluation

Finally, we also evaluated the 3D TRE, i.e. the estimated position in the MRI of the landmarks in the mammograms. We used the algorithm proposed by García et al. (2017), which allows locating the lesion position within the MRI without uncompressing the breast models. We test the 3D error registration for every similarity metric. For each landmark in the FFDM, the X-ray path is computed, from the source to the marker. Barycentric coordinates are computed in the tetrahedrons traversed by the ray, and the list of elements and barycentric coordinates is used to localize the two curves within the MRI. The center of mass between the two closest points is considered the 3D position of the landmark. Thus, the TRE is computed as the Euclidean distance between the centroid of the real landmark and the estimated position from the FFDMs.

Tables 5 and 6 summarize the 3D TRE using both isotropic and transversally isotropic material models. Notice that the 3D TRE should be related to the breast model behavior because two different material models yield a different distribution of the internal space. For the isotropic material model, the best performance is obtained using the scalar gradient values (10.13 ± 7.09 mm) and, similarly, using the anisotropic material model (7.33 ± 3.62). The worst performance using the isotropic material model is obtained by the intensity-based methods (11.09 ± 2.77), while the algorithm using vectoral gradient values yields the worst result for the anisotropic material model (10.49 ± 5.11).

3.5. Factors of influence

In this section we analyze different factors that can influence the performance of the registration algorithms. Due to the previous results, we focused our attention on the method using a scalar gradient value, since this approach obtained the best performance in most of the cases.

The first limiting factor may be related with the glandularity -i.e. ratio between glandular tissue and breast volume- of the breast. In this work, we assumed that the breast is composed of one single material. However, the breast is composed mainly of glandular and adipose tissue. The Young's modulus, measured by Wellman, for glandular and adipose tissue is 4.46 kPa and 15.1 kPa, respectively. Therefore, the mechanical behavior of the breast can be related to the glandularity. Volumetric breast density (VBD) was computed using the commercial software Volpara™[5] (Volpara Health Technologies Ltd., Wellington, New Zealand) directly from the "for processing" (raw) mammograms. Fig. 7 shows the TRE, in millimeters, versus the glandularity of the breast, in volumetric percentage, considering the error obtained from the gradient-based registration algorithm that uses the scalar gradient value. For CC images, the correlation is $R = 0.56$ (absolute value), while for MLO images, there is no clear correlation ($R = 0.13$) between the values.

A second factor of influence in the TRE could be the landmark position within the breast. Lesions localized close to the pectoral muscle have a more constrained movement than the lesions situated close to the skin. Therefore, the TRE may be smaller when the lesion is close to the pectoral. Considering this fact, we investigate the correlation between the TRE and the distance from the lesion to the pectoral muscle. Fig. 8 shows the TRE with respect to the distance between the landmark and the pectoral muscle presented in the mammogram for both CC- and MLO- projections. In the CC-projections for the whole dataset, the correlation is $R = 0.77$, while for MLO images, $R = 0.50$ using the scalar gradient value. The TRE is not only involved in the constrained movement of the landmarks localized closer to the pectoral muscle but, also, to the biomechanical model behavior. This fact is also related to the description of the breast model as one single material, and an accurate description of the internal breast tissues may reduce the correlation values.

Apart from the distance to the pectoral muscle, the own position of the landmarks can affect the TRE. Notice that using the transversal isotropic material model, the stiffer direction has been defined in the perpendicular direction to the pectoral muscle. Therefore, the most affected direction is the perpendicular direction from the pectoral muscle to the farthest point in the perpendicular direction that corresponds to the nipple. Thus, using these two anatomical landmarks of the breast, an internal system of reference can be defined. Each lesion can be localized, using polar

[5] http://www.volparasolutions.com/.

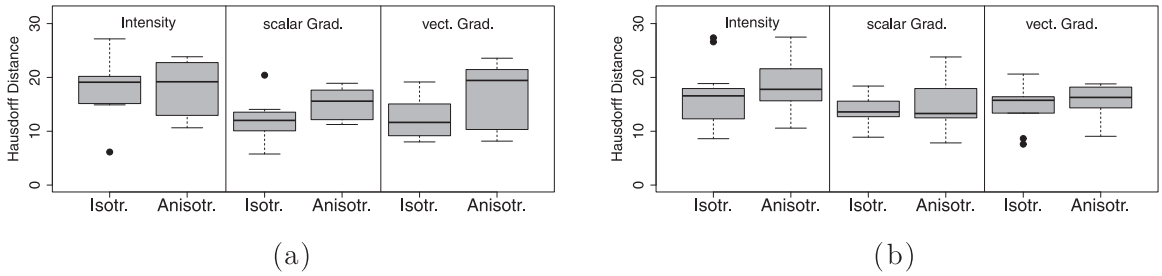

Fig. 6. Hausdorff distances between the real and projected breast contours, for CC- (a) and MLO-projections (b).

Table 6
3D Target registration error, in millimeters, within the MRI, using a traversal isotropic material model.

	c1	c2	c3	c4	c5	c6	c7	c8	c9	c10	mean	std
Intensity	10.41	3.95	5.07	11.21	5.67	15.61	9.19	2.14	4.31	10.51	7.81	4.21
scalar Grad.	11.50	9.25	8.35	4.67	7.88	11.65	10.40	4.56	0.71	4.32	7.33	3.62
vect. Grad.	8.63	7.53	18.07	7.72	11.57	5.13	14.47	19.06	4.96	7.76	10.49	5.11

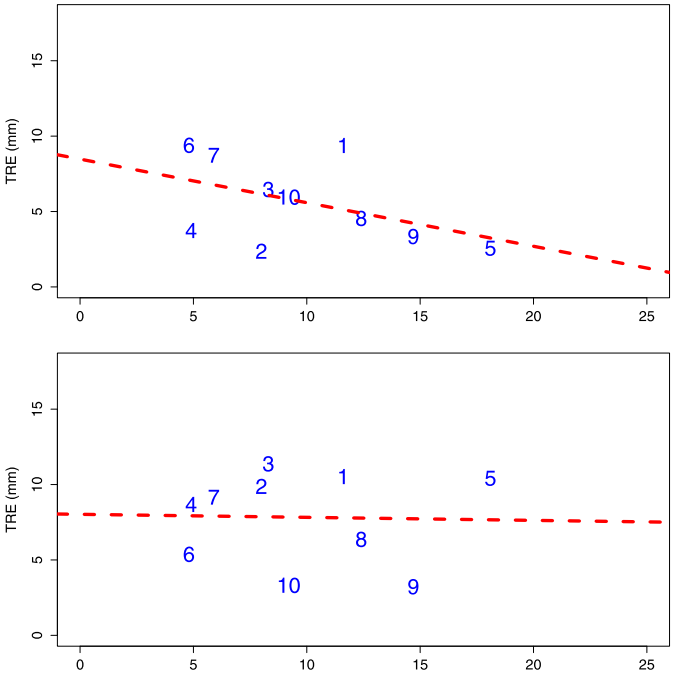

Fig. 7. Target registration error, in millimeters, with respect to the volumetric breast density, in percentage, for CC- (top) and MLO- (bottom) projections.

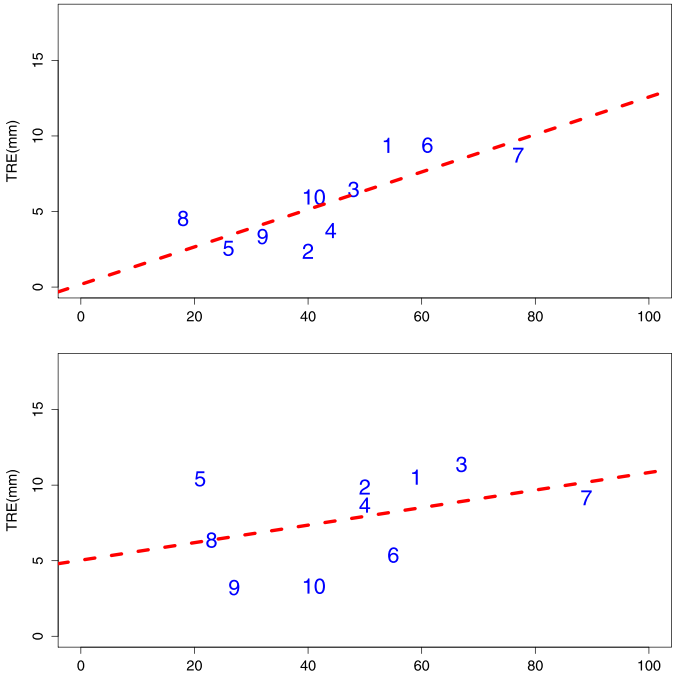

Fig. 8. Target registration error, in millimeters, with respect to the distance from the pectoral muscle to the landmark for both CC- (top) and MLO- (bottom) mammograms, in millimeters.

coordinates, by the radius, ρ, and the angle, ϕ, in the internal system of reference. Fig. 9 shows the position of the ten landmarks composing the dataset using the proposed system of reference. The breast shape is represented by a semi-circle with radius $R = 1$, normalized using the distance from the pectoral muscle to the nipple for each case. Thus, we can evaluate not only the lesion position with respect to the pectoral muscle but, also, the relative position of the lesion within the breast. Considering this system of reference, the TRE can be evaluated with respect to the deviation of the principal direction, using the coordinate ϕ. Fig. 10 shows the scatter plot of the TRE, in millimeters, with respect to the angle, ϕ, in degrees, obtained using the internal system of reference and cylindrical coordinates. Using real values for describing the angle the correlation is $R = 0.34$. When the ϕ is considered in absolute value, the correlation increases to $R = 0.65$. Regarding the MLO projections, in the two cases, using the real and absolute value of ϕ, the algorithm does not show a significant correlation (smaller than $R = 0.40$).

4. Discussion

The aim of this paper was to introduce two gradient-based methods for breast MRI to X-ray mammography registration, comparing their results with a traditional intensity-based approach. We presented a fully automatic framework to register these image modalities using a patient-specific biomechanical model, extracted from the MRI with the aim of mimicking the mammographic acquisition. In the intensity-based approach, the MRI images were transformed to pseudo-CT images, considering the tissue segmentation and the parameters used to acquire the mammography, while normalized cross-correlation was used to lead the registration process. In the gradient-based algorithms, the intensity gradients were extracted in the MRI volume and projected into the

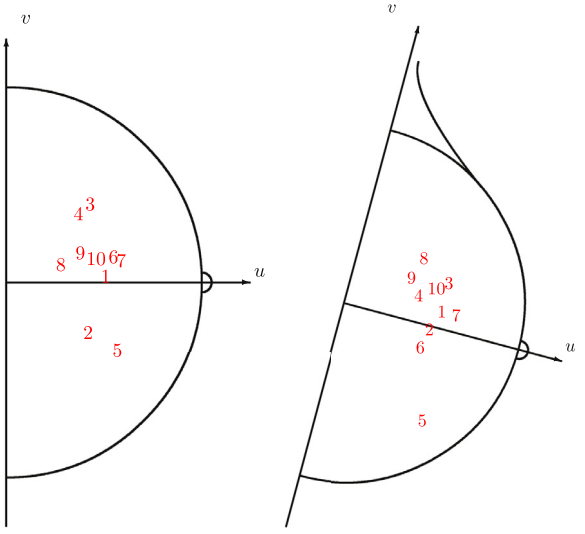

Fig. 9. Landmark position for the ten cases in the CC- (left) and MLO- (right) projections corresponding to the clinical dataset. Notice that the generic breast model is represented as a left breast while the dataset contains both left and right breast images.

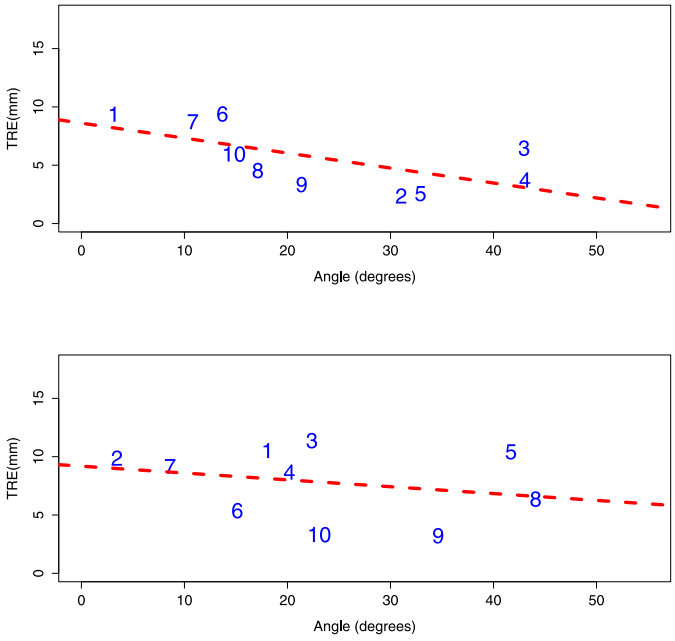

Fig. 10. Target registration error, in millimeters, with respect to the absolute angle value, $abs(\phi)$, in degrees, obtained using the internal system of reference and polar coordinates for both CC- (top) and MLO- (bottom) mammograms.

mammographic space. Thus, NCC of the scalar gradients values and gradient correlation of the vectoral gradients were used to perform the optimization. Finally, we evaluated the accuracy of the registration using the target registration error approach between landmarks, comparing the results among the three algorithms.

The results were obtained testing both isotropic and anisotropic material models. In general, using the anisotropic model showed a better performance, reducing the TRE obtained by using the isotropic biomechanical models, especially for the intensity-based and the scalar gradient methods. However, when using the vectoral gradient similarity, the results do not show such a large improvement. Regarding the registration methods, the use of scalar gradient values did not only obtain the best result among the gradient-based methods but also improved the TRE obtained by the intensity-based method. A similar behavior is observed when evaluating the 3D TRE. The 3D TRE should be related, also, to the 2D TRE of the two mammographic views, obtaining better results when the accuracy of the 3D-2D registration is higher. This rule seems to be established in most of the cases. However, the internal deformation of the model may vary these results depending on the breast material model.

In contrast to intensity-based methods, where the amount of glandular tissue provided by the segmentation may vary the final registration result, gradient-based methods take into consideration the parenchymal distribution, regardless of the tissue segmentation step. García et al. (2018b) reported that there is a structural similarity of the glandular tissue obtained from the MRI and the mammographic images. However, in the same work, it is reported that, even when there is a similarity between the information of the two image modalities, the amount of glandular tissue is not the same. We consider that this is the main reason for the improvement obtained by the gradient-based method.

Similarly, the results exposed in Section 3.3 show a better performance of the isotropic mechanical model when the distance between the real and the projected contour is computed. The images obtained during this process show that the breast shape is better fitted by an isotropic model instead of an anisotropic model. Breast shape is determined by the interaction between the mechanical model description and external loads. Shape and internal tissue movement are tightly coupled in the biomechanical analysis. Therefore, these result may result surprising. The source of these divergences may correspond to the internal landmark position. As we exposed during this work, the stiffest direction of the anisotropic material models corresponds the direction perpendicular to the pectoral muscle, traversing the nipple. A deeper analysis shows that the landmarks are situated within the interval of -45 and 45 degrees with respect to this direction (see Fig. 10), which represents a more constraint movement than those areas localized close to the skin. Moreover, the Hausdorff distance computes the maximum distance between two curves. Even when the curve is well fitted close to the nipple, the breast shape obtained by the anisotropic mechanical model may be deformed in both sides of the contour, corresponding to the sternum and axillar area, increasing the computed distance. These small divergences between the two contours are shown in Fig. 5. On the other hand, we need to take into consideration that intensity-based metrics, such as NCC, represent non-convex topologies during the optimization of the model position and, therefore, the model may not obtain an accurate position during the optimization step, reaching a suboptimal solution.

The main goal of the gradient-based method using scalar values is to localize areas with high gradient difference in a similar position, while using vectoral gradient values involves also a spatial -i.e. directional- consideration. Therefore, the former approach may be less affected by factors such as the difference between the images, MRI and mammogram resolution, unsuitable or inaccurate internal tissue deformation (due to the use of one single material model instead of multiple tissues). However, the algorithm that uses the vectoral gradient values approach may require a more accurate simulation. Notice, for instance, that the smaller the pixel size, the smaller the difference between the intensity values between neighbors and, therefore, the smaller the gradient obtained. The difference between the MRI voxel and the mammographic pixel sizes may affect the directionality of the gradient vectors that lead the registration. Additionally, the physics underlying each image modality is different and the internal structures presented in one of the modalities may not be visible in the other. As we showed previously, there is a similarity between MRI and X-ray mammography images, but the information obtained from the two images modalities is not the same. For instance, nerves or vessels

that are not shown in the MRI may affect the result. We consider that these may be the source of the different behavior using scalar and vectoral gradient values during the registration as well as the reason why the approach that uses vectoral values does not obtain a clear improvement when the anisotropic material model is considered.

Moreover, we have studied different factors that may influence the evaluation, such as the glandularity and the relative position of the landmark within the breast. Several linear relationship, with a moderate correlation, have been observed for the gradient-based algorithms. However, notice that in most of the cases there is not a clear correlation, taking each approach independently, and one should be cautious considering these values. The small number of cases leads to inconclusive results on how the landmark position may alter the final result. Our results, obtained by gradient-based methods, do not show a clearly significant difference with respect to the traditional intensity-based registration algorithm. Even when there is a clear improvement, on average, the use of a small dataset avoids providing an accurate result in term of significance of the results.

With respect to the divergences considering the CC- and MLO-projections, we consider that the image acquisition affects the final result of the registration. Note that in previous work (García et al., 2018b), we also obtained a different behavior for CC- and MLO-projections. While during the CC acquisition, the breast is easily situated with respect to the mammographic space, during the MLO acquisition, the initial position of the breast model depends on the pectoral muscle segmentation and the rotation in the anterior-posterior direction (usually 45 degrees with respect to the vertical). Defining a suitable initial position is mandatory to obtain an accurate result. The optimization step reduces the difference between the breast model and the real position during the mammographic acquisition. However, the model may not obtain an accurate position during the optimization step, yielding the divergences between the TRE of the two mammographic projections.

The main limitation of this work is the small dataset (10 cases). Even when this value is in the range with previous works in MRI-mammography registration (Ruiter et al., 2003, 6 cases; Lee et al., 2013, 5 CC and 4 MLO-projections; Solves-Llorens et al., 2014, 14 patients; and Mertzanidou et al., 2014, 10 CC and MLO cases), the registration accuracy, as well as the correlation between the TRE and the exposed factors, may vary using a larger dataset. Furthermore, the relative landmark position, represented in Fig. 9, shows that most of the landmarks are localized close to the center and in the upper half side of the breast, which is clearly related to the glandular tissue distribution. In the breast, the lobules branch out from the nipple and are linked by a network of ducts. Furthermore, for denser breasts, the glandular tissue can reach up to the axila. Therefore, in the mammograms of the left breast, as is represented in the generic model in Fig. 9, the glandular tissue is projected in the upper half side of the image. Thus, most of the landmarks are situated within or close to the glandular tissue where the sensitivity of the mammographic images can decrease.

However, similar to intensity-based approaches, several disadvantages need to be considered in the gradient-based approaches. MRI artifacts, such as a poor bias field correction, skin folding, or a poor delineation of the skin, can modify the final registration results. Furthermore, the poor contrast between glandular and adipose tissue in the “for presentation” mammograms, obtained by means of the GE healthcare devices, as is shown in Fig. 2, forces us to use a histogram equalization to increase the difference between the two tissues. This fact has a notable influence in the final registration result. However, using images from other vendor machines may allow skipping this step.

Finally, on average, the computational time of the registration (after extracting the biomechanical model) is approximately one hour. This value is lower than the values reported by Mertzanidou et al. (2014) and Hopp et al. (2013). Note that these works were proposed several years ago and, neither the hardware nor the software is the same in all cases. Therefore, with actual facilities their approaches should run faster, improving their reported time values. Much of the time is waisted in the interface between NiftySim^{TM} and the registration software, while the rest of the algorithm (ray-casting, model transformation and optimization) is integrated in the software. The FE analysis and the ray-casting is accelerated with GPU, using just 128 threads which is smaller than the maximum number of threads per block in the current graphic cards. Furthermore, an atlas-based approach has been used to separate the breast from the body, and a region-growing algorithm, to remove the background of the image, taking advantage of previous work (Gubern-Mérida et al., 2014). However, some other approaches can be tested to isolate the breast (Wang et al., 2012; Wu et al., 2013), avoiding intensity-based segmentation algorithms and reducing the computational time. Therefore, other implementations, that also include an integrated FE solver, may reduce the computational time for this process, allowing us to reach an assumable time in the clinical practice.

5. Conclusions

In this paper, we have introduced two gradient-based registration algorithms to lead the breast MRI and X-ray mammography registration. The best results have been obtained using scalar gradient values and the normalized cross-correlation, outperforming the results obtained by using an intensity-based method. Furthermore, the target registration error shows a moderate correlation with respect to the glandularity as well as the landmark position within the breast.

The accuracy of the presented registration approach, in the order of 10 mm, could provide valuable information to radiologists. Our approach reduce the target registration error to half a centimeter allowing an assumable error in the clinical practice with the aim of localizing susceptible areas within the MRI or the mammogram from the other image modality.

Conflict of interest

There are no conflicts of interest.

Acknowledgment

This research has been partially supported from the University of Girona (MPC UdG 2016/022 grant), the European Union within the Marie Sklodowska-Curie Innovative Training Networks (SCARtool project H2020-MSCA-IF-2014, reference 657875) and the Ministry of Economy and Competitiveness of Spain, under project SMARTER (DPI2015-68442-R) and the FPI grant BES-2013-065314.

References

Azar, F.S., Metaxas, D.N., Schnall, M.D., 2001. A deformable finite element model of the breast for predicting mechanical deformations under external perturbations. Acad. Radiol. 8 (10), 965–975.

Van der Bom, M., Pluim, J., Gounis, M., van de Kraats, E., Sprinkhuizen, S., Timmer, J., Homan, R., Bartels, L., 2011. Registration of 2D x-ray images to 3D MRI by generating pseudo-CT data. Phys. Med. Biol. 56 (4), 1031.

Bonet, J., Wood, R., 1997. Nonlinear Continuum Mechanics for Finite Element Analysis. Cambridge University Press.

Boone, J.M., Fewell, T.R., Jennings, R.J., 1997. Molybdenum, rhodium, and tungsten anode spectral models using interpolating polynomials with application to mammography. Med. Phys. 24 (12), 1863–1874.

BreastCancer.org, 2017. BreastCancer.org, url: http://www.breastcancer.org/symptoms/testing/types.

Chung, 2008. Modelling mammographic mechanics. University of Auckland, New Zealand Phd thesis.

Eiben, B., Vavourakis, V., Hipwell, J.H., Kabus, S., Lorenz, C., Buelow, T., Hawkes, D.J., 2014. Breast deformation modelling: comparison of methods to obtain a patient specific unloaded configuration. In: In SPIE Medical Imaging: Image-Guided Procedures, Robotic Interventions, and Modeling, Vol. 9036, p. 903615.

Fiaschetti, V., Pistolese, C., Funel, V., Rascioni, M., Claroni, G., Della Gatta, F., Cossu, E., Perretta, T., Simonetti, G., 2013. Breast MRI artefacts: evaluation and solutions in 630 consecutive patients. Clin. Radiol. 68 (11), e601–e608.

Fung, Y., 1993. Biomechanics: Mechanical Properties of Living Tissues, 2nd Springer.

Gan, R., Chung, A.C., Liao, S., 2008. Maximum distance-gradient for robust image registration. Med. Image Anal. 12 (4), 452–468.

García, E., Diez, Y., Diaz, O., Lladó, X., Gubern-Mérida, A., Martí, R., Martí, J., Oliver, A., 2018b. Multimodal breast parenchymal patters correlation using a patient-specific biomechanical model. IEEE Trans. Med. Imaging 37 (3), 712–723.

García, E., Diez, Y., Diaz, O., Lladó, X., Martí, R., Martí, J., Oliver, A., 2018a. A step-by-step review on patient-specific biomechanical finite elements models for breast MRI to x-ray mammography registration. Med. Phys. 45 (1), e6–e31.

García, E., Oliver, A., Diez, Y., Diaz, O., Georgii, J., Gubern-Mérida, A., Martí, J., Martí, R., 2015. Comparing Regional Breast Density Using Full-field Digital Mammograms and Magnetic Resonance Imaging: a Preliminary Study. In: MICCAI Workshop on Breast Image Analysis, pp. 33–41.

García, E., Oliver, A., Diez, Y., Diaz, O., Gubern-Mérida, A., Martí, R., Martí, J., 2017. Mapping 3D Breast Lesions from Full-field Digital Mammograms Using Subject-specific Finite Element Models. In: SPIE Medical Imaging, Proc. SPIE, Vol. 10135, pp. 1013504O1–1013504O8.

Gubern-Mérida, A., Kallenberg, M., Martí, R., Karssemeijer, N., 2012. Segmentation of the pectoral muscle in breast MRI using atlas-based approaches. Medical Image Computing and Computer-Assisted Intervention, MICCAI. Springer Berlin Heidelberg..

Gubern-Mérida, A., Kallenberg, M., Platel, B., Mann, R., Martí, R., Karssemeijer, N., 2014. Volumetric breast density estimation from full-field digital mammograms: a validation study. PLoS One e85952.

Han, L., Hipwell, J., Tanner, C., Taylor, Z., Mertzanidou, T., Cardoso, J., Ourselin, S., Hawkes, D., 2012. Development of patient-specific biomechanical models for predicting large breast deformation. Phys. Med. Biol. 57 (2), 455–472.

Herrmann, L.R., 1976. Laplacian-isoparametric grid generation scheme. J. Eng. Mech. Div. 102 (5), 749–907.

Hopp, T., Dietzel, M., Baltzer, M., Kaiser, W., Gemmeke, H., Ruiter, N., 2013. Automatic multimodal 2d/3d breast image registration using biomechanical FEM models and intensity-based optimization. Med. Image Anal. 17, 209–218.

Hopp, T., Duric, N., Ruiter, N., 2012. Automatic multimodal 2D/3D image fusion of ultrasound computer tomography and x-ray mammography for breast cancer diagnosis. In: Proc. SPIE Medical Imaging, Vol. 8320. 8320-1–8

Hopp, T., Ruitter, N., 2012. 2D/3D registration for localization of mammographycally depicted lesions in breast MRI. Lect. Notes Comput. Sci. 7361, 627–634.

Johnsen, S., Taylor, Z.A., Clarkson, M., Hipwell, J., Modat, M., Eiben, B., Han, L., Hu, Y., Mertzanidou, T., Hawkes, D.J., Ourselin, S., 2014. Niftysim: a gpu-based nonlinear finite element package for simulation of soft tissue biomechanics. J. Comput. Assisted Radiol. Surg..

Kirkpatrick, S., Vecchi, M.P., et al., 1983. Optimization by simmulated annealing. Science 220 (4598), 671–680.

Kwok, S.M., Chandrasekhar, R., Attikiouzel, Y., Rickard, M.T., 2004. Automatic pectoral muscle segmentation on mediolateral oblique view mammograms. IEEE Trans. Med. Imaging 23 (9), 1129–1140.

Lagae, A., Dutré, P., 2008. Compact, fast and robust grids for ray tracing. Comput. Graphics Forum 27 (4), 1235–1244.

Lee, A., Rajagopal, V., Gamage, T.B., Doyle, A., Nielsen, P., Nash, M., 2013. Breast lesion co-localisation between X-ray and MR images using finite element modelling. Med. Image Anal. 17, 1256–1264.

Livyatan, H., Yaniv, Z., Joskowicz, L., 2003. Gradient-based 2-D/3-D rigid registration of fluoroscopic X-ray to CT. IEEE Trans. Med. Imaging 22 (11), 1395–1406.

Lorensen, W., Cline, H., 1987. Marching cubes: a high resolution 3D surfaces construction algorithm. ACM Comput. Graphics 21 (4), 163–169.

Markelj, P., Tomaževic, D., Pernuš, F., Likar, B., 2008. Robust gradient-based 3-D/2-D registration of CT and MR to X-ray images. IEEE Trans. Med. Imaging 27 (12), 1704–1714.

Mertzanidou, T., Hipwell, J., Johnsen, S., Han, L., Einben, B., Taylor, Z., Ourselin, S., Huisman, H., Mann, R., Bick, U., Kaissermeijer, N., Hawkes, D.J., 2014. MRI to X-ray mammography intensity-based registration with simultaneous optimisation of pose and biomechanical transformation parameters. Med. Image Anal. 18 (4), 674–683.

Mertzanidou, T., Hipwell, J., Tanner, C., Hawkes, D., 2010. An intensity-based approach to x-ray mammography–MRI registration. In: Proc. SPIE Medical Imaging, Vol. 7623. 7623-1–8

Mertzanidou, T., Hipwell, J., Cardoso, M.J., Zhang, X., Tanner, C., Ourselin, S., Bick, U., Huisman, H., Karssemeijer, N., Hawkes, D., 2012. Mri to x-ray mammography registration using a volume-preserving affine transformation. Med. Image Anal. 16 (5), 966–975.

Otsu, N., 1975. A threshold selection method from gray-level histograms. Automatica 11 (285–296), 23–27.

Pluim, J.P., Maintz, J.A., Viergever, M.A., 2000. Image registration by maximization of combined mutual information and gradient information. In: International Conference on Medical Image Computing and Computer-Assisted Intervention. Springer, Berlin, Heidelberg, pp. 452–461.

Ruiter, N., Müller, T., Stotzka, R., Gemmeke, H., Reichenbach, J., Kaiser, W., 2003. Finite element simulation of the breast's deformation during mammography to generate a deformation model for registration. In: Informatik aktuell - Bildverarbeitung fur die Medizin, pp. 86–90.

Ruiter, N., Stotzka, R., Müller, T.O., Gemmeke, H., Reichenbach, J.R., Kaiser, W.A., 2006. Model-based registration of X-ray mammograms and MR images of the female breast. IEEE Trans. Nucl. Sci. 53 (1), 204–211.

Si, H., 2015. Tetgen. a delaunay-based quality tetrahedral mesh generator. ACM Trans. Math. Softw. 41 (2), 11.

Solves-Llorens, J.A., Rupérez, M., Monserrat, C., 2014. A complete software application for automatic registration of X-ray mammography and magnetic resonance images. Med. Phys. 41 (8).

Tanner, C., Degenhard, A., Schnabel, J., Smith, A.C., Hayes, C., Sonoda, L., Leach, M., Hose, D., Hill, D., Hawkes, D., 2001. A method for the comparison of biomechanical breast models. In: Mathematical Methods in Biomedical Image Analysis, 2001 MMBIA 2001. IEEE Workshop on. IEEE, pp. 11–18.

Tomaževič, D., Likar, B., Slivnik, T., Pernuš, F., 2003. 3-D/2-D registration of CT and MR to X-ray images. IEEE Trans. Med. Imaging 22 (11), 1407–1416.

Wang, L., Platel, B., Ivanovskaya, T., Harz, M., Hahn, H.K., 2012. Fully automatic breast segmentation in 3D breast MRI. In: Biomedical Imaging (ISBI), 2012 9th IEEE International Symposium on. IEEE, pp. 1024–1027.

Wein, W., Röper, B., Navab, N., 2005. 2D/3D registration based on volume gradients. In: Medical Imaging. International Society for Optics and Photonics, pp. 144–150.

Wellman, P., 1999. Tactile Imaging. Cambridge, MA: Harvard University's Division of Engineering and Applied Sciences Ph.d. thesis.

Wu, S., Weinstein, S.P., Conant, E.F., Schnall, M.D., Kontos, D., 2013. Automated chest wall line detection for whole-breast segmentation in sagittal breast MR images. Med. Phys. 40 (4).